Monthly Notices
of the
ROYAL ASTRONOMICAL SOCIETY

Mon. Not. R. Astron. Soc. **421,** 2917–2929 (2012) doi:10.1111/j.1365-2966.2012.20520.x

The dust and gas properties of M83

K. Foyle,[1⋆] C. D. Wilson,[1] E. Mentuch,[1] G. Bendo,[2] A. Dariush,[3] T. Parkin,[1] M. Pohlen,[4] M. Sauvage,[5] M. W. L. Smith,[4] H. Roussel,[6] M. Baes,[7] M. Boquien,[8] A. Boselli,[8] D. L. Clements,[3] A. Cooray,[9] J. I. Davies,[4] S. A. Eales,[4] S. Madden,[5] M. J. Page[10] and L. Spinoglio[11]

[1]*Department of Physics & Astronomy, McMaster University, Hamilton, Ontario L8S 4M1, Canada*
[2]*UK ALMA Regional Centre Node, Jodrell Bank Centre for Astrophysics, School of Physics and Astronomy, University of Manchester, Oxford Road, Manchester M13 9PL*
[3]*Astrophysics Group, Imperial College, Blackett Laboratory, Prince Consort Road, London SW7 2AZ*
[4]*School of Physics & Astronomy, Cardiff University, Queen Buildings, The Parade, Cardiff CF24 3A*
[5]*CEA, Laboratoire AIM, Irfu/SAp, Orme des Merisiers, F-91191 Gif-sur-Yvette, France*
[6]*Institut d'Astrophysique de Paris, UMR7095 CNRS, Université Pierre & Marie Curie, 98 bis Boulevard Arago, F-75014 Paris, France*
[7]*Sterrenkundig Observatorium, Universiteit Gent, Krijgslaan 281 S9, B-9000 Gent, Belgium*
[8]*Laboratoire d'Astrophysique de Marseille, UMR6110 CNRS, 38 rue F. Joliot-Curie, F-13388 Marseille, France*
[9]*Department of Physics & Astronomy, University of California, Irvine, CA 92697, USA*
[10]*Mullard Space Science Laboratory, University College London, Holmbury St Mary, Dorking, Surrey RH5 6NT*
[11]*Istituto di Fisica dello Spazio Interplanetario, INAF, Via del Fosdso del Cavaliere 100, I-00133 Roma, Italy*

Accepted 2012 January 8. Received 2011 December 22; in original form 2011 October 31

ABSTRACT

We examine the dust and gas properties of the nearby, barred galaxy M83, which is part of the Very Nearby Galaxy Survey. Using images from the Photodetector Array Camera and Spectrometer (PACS) and Spectral and Photometric Imaging REceiver (SPIRE) instruments of *Herschel*, we examine the dust temperature and dust mass surface density distribution. We find that the nuclear, bar and spiral arm regions exhibit higher dust temperatures and masses compared to interarm regions. However, the distributions of dust temperature and mass are not spatially coincident. Assuming a trailing spiral structure, the dust temperature peaks in the spiral arms lie ahead of the dust surface density peaks. The dust mass surface density correlates well with the distribution of molecular gas as traced by CO ($J = 3 \rightarrow 2$) images (James Clerk Maxwell Telescope) and the star formation rate as traced by Hα with a correction for obscured star formation using 24-μm emission. Using H I images from The H I Nearby Galaxy Survey (THINGS) to trace the atomic gas component, we make total gas mass surface density maps and calculate the gas-to-dust ratio. We find a mean gas-to-dust ratio of 84 ± 4 with higher values in the inner region assuming a constant CO-to-H_2 conversion factor. We also examine the gas-to-dust ratio using CO-to-H_2 conversion factor that varies with metallicity.

Key words: galaxies: individual: M83 – galaxies: ISM – galaxies: spiral – infrared: galaxies.

1 INTRODUCTION

Dust emission represents approximately one-third of the bolometric luminosity in normal spiral galaxies and dust acts to shape the spectral energy distribution (SED) of galaxies by attenuating short-wavelength emission and re-emitting at longer wavelengths. Dust can also be used to trace the total gas content in galaxies, since dust and gas often coexist. An understanding of dust and its distribution is essential to reveal the underlying appearance of galaxies and the processes within (Draine 2003).

Until recently, it has been difficult to map the distribution and amount of dust in galaxies because, for most galaxies, only shorter wavelength infrared data have been available (i.e. $\lambda < 160\,\mu$m). Without longer wavelengths, only the warmer dust emission is measured and subsequently the dust mass is poorly constrained (Draine et al. 2007; Galametz et al. 2011). While some ground-based telescopes [i.e. Submillimetre Common-User Bolometer Array (SCUBA) on James Clerk Maxwell Telescope (JCMT); Holland et al. 1999, and the bolometer camera SHARC-II on the Caltech Submillimeter Observatory (CSO); Dowell et al. 2003]

⋆E-mail: foylek@physics.mcmaster.ca

© 2012 The Authors
Monthly Notices of the Royal Astronomical Society © 2012 RAS

have provided measurements in the far-infrared (350, 450 and 850 μm) allowing for more accurate dust SED fits (e.g. Dunne et al. 2000; Dunne & Eales 2001; Dale et al. 2007); these images had low sensitivity due to background noise from the atmosphere.

The *Herschel Space Observatory* (Pilbratt et al. 2010) has allowed us to probe the colder dust component in galaxies using measurements at wavelengths spanning 70–500 μm at high sensitivity and resolution. In comparison to the *Spitzer Space Telescope* (Werner et al. 2004), which also operated at 70 and 160 μm (Multiband Imaging Photometer, MIPS; Rieke et al. 2004), the point spread functions (PSFs) are smaller, the sensitivity is higher and there are fewer latent image effects.

In this work, we use *Herschel* observations to make dust temperature and mass maps for M83 which is part of the Very Nearby Galaxy Survey (VNGS; PI: C. Wilson). Due to its proximity (4.5 ± 0.3 Mpc; Thim et al. 2003), which allows for high spatial resolution, and its relatively face-on orientation (inclination angle of 24°), it makes an excellent candidate to study the spatial distribution of the dust mass and temperature.

M83 is a starburst galaxy with a prominent bar, which is outlined by dust lanes. Dynamical studies have shown that gas is funnelled along the bar producing high rates of star formation at the centre (Knapen et al. 2010). M83 is rich in molecular gas with 13 per cent of the disc mass consisting of molecular gas (Lundgren et al. 2004). Studies of the spiral arms have shown that tracers of the gas and star formation rate (SFR) are often offset from each other suggesting that the spiral arms dynamically induce star formation (Lord & Kenney 1991). However, the situation is complicated in that molecular clouds are also seen coincident with young star-forming regions (Rand, Lord & Higdon 1999). Studies of the mid-infrared emission, which traces the very small dust grains and polycyclic aromatic hydrocarbons (PAHs), have revealed a tight correlation with the radio continuum, which may suggest the anchoring of magnetic fields in the photoionizing shells of clouds (Vogler et al. 2005). The morphology of M83 and the fact that it has coverage at many other wavelengths allow for comparisons of the varying environments within the galaxy and comparisons of the dust distribution to tracers of the gas and SFR.

We estimate the dust temperature and mass of M83 on angular scales of 36 arcsec (790 pc) using 70- and 160-μm images from the Photodetector Array Camera and Spectrometer (PACS; Poglitsch et al. 2010) and the 250-, 350-, 500-μm maps from the Spectral and Photometric Imaging REceiver (SPIRE; Griffin et al. 2010). We compare the spatial distribution of the dust temperature and mass with tracers of the atomic gas, molecular gas and SFR for different regions in the galaxy including the nucleus, bar and spiral arms. In Section 2 we describe how the infrared, gas and SFR images were rendered and processed. Our derivation of the dust temperature and dust mass distributions through SED fitting on each pixel is described in Section 3, and compared to the distributions of molecular and total gas as well as the SFR surface density in Section 4. Our conclusions are summarized in Section 5.

2 OBSERVATIONS AND IMAGE RENDERING

2.1 *Herschel* images

We use PACS images that are processed using both HIPE v5 and SCANAMORPHOS v8[1] (Roussel 2012), and SPIRE images processed with HIPE and BRIGADE (Smith et al., in preparation). Details on how the images are processed can be found in Bendo et al. (2012), the SPIRE Observer's Manual[2] and the PACS Observer's Manual.[3] We briefly describe the steps here. The PACS images were corrected from the v5 photometric calibration files to v6 (with corrective factors of 1.119 and 1.174 for the 70- and 160-μm maps, respectively) and were converted to Jy sr^{-1} from Jy pixel^{-1}. The SPIRE images are first converted to Jy pixel^{-1} from Jy beam^{-1} using the respective beam sizes (423 ± 3, 751 ± 4, 1587 ± 9 arcsec^2, for the 250-, 350- and 500-μm images, respectively). The images were then converted to Jy sr^{-1}. The SPIRE images were multiplied by the following values to convert from monochromatic intensities of point sources to monochromatic extended sources, 0.9939/1.0113, 0.9898/1.0060 and 0.9773/1.0065 for the 250-, 350- and 500-μm maps, respectively. Table 1 lists the pixel sizes and full width at half-maximum (FWHM) of the PSFs for both the PACS and SPIRE images. Sky subtractions for all five images were made by subtracting the median value of several off-galaxy apertures. Fig. 1 shows the five images in their native resolution, before convolution and deprojection.

Table 1. Characteristics of images.

Image	Pixel size (arcsec)	FWHM of PSF (arcsec)
70 μm	1.4	6.0
160 μm	2.85	12.0
250 μm	6	18.2
350 μm	8	24.5
500 μm	12	36.0

The images are all aligned and convolved to the 500-μm images using kernels developed by Aniano et al. (2011) for PACS and SPIRE. The final pixel size is 12 arcsec. However, in our quantitative analysis we use 36-arcsec pixels, which correspond to the FWHM of the 500-μm map. We also deproject the images to a face-on orientation adopting the inclination and position angles from Tilanus & Allen (1993) (see Table 2).

The uncertainties for each image are a combination of the uncertainty image files, which are corrected for convolution and deprojection, sky background uncertainties and the calibration uncertainties (0.03, 0.05, 0.07, 0.07, 0.07 for the calibration uncertainties of the 70-, 160-, 250-, 350- and 500-μm images respectively).

While MIPS images from *Spitzer* (Rieke et al. 2004) are available for M83 at 70 and 160 μm, they suffer from latent image effects and saturation in the nucleus due to M83's brightness (see Bendo et al. 2012, for a discussion). Thus, we choose not to include these images in our analysis.

2.2 H I, CO and gas maps

We use 21-cm line emission maps from The H I Nearby Galaxy Survey (THINGS; Walter et al. 2008) to trace the atomic gas. We use the natural weighted maps with a resolution of 13 arcsec and convert the integrated intensity to a surface density following Leroy et al. (2008). The H I maps are aligned and convolved to match the 500-μm images and are deprojected according to the values in Table 2.

[1] SCANAMORPHOS Documentation: http://www2.iap.fr/users/roussel/herschel/

[2] SPIRE Observer's Manual: http://herschel.esac.esa.int/Docs/SPIRE/html/spire_om.html

[3] PACS Observer's Manual: http://herschel.esac.esa.int/Docs/PACS/html/pacs_om.html

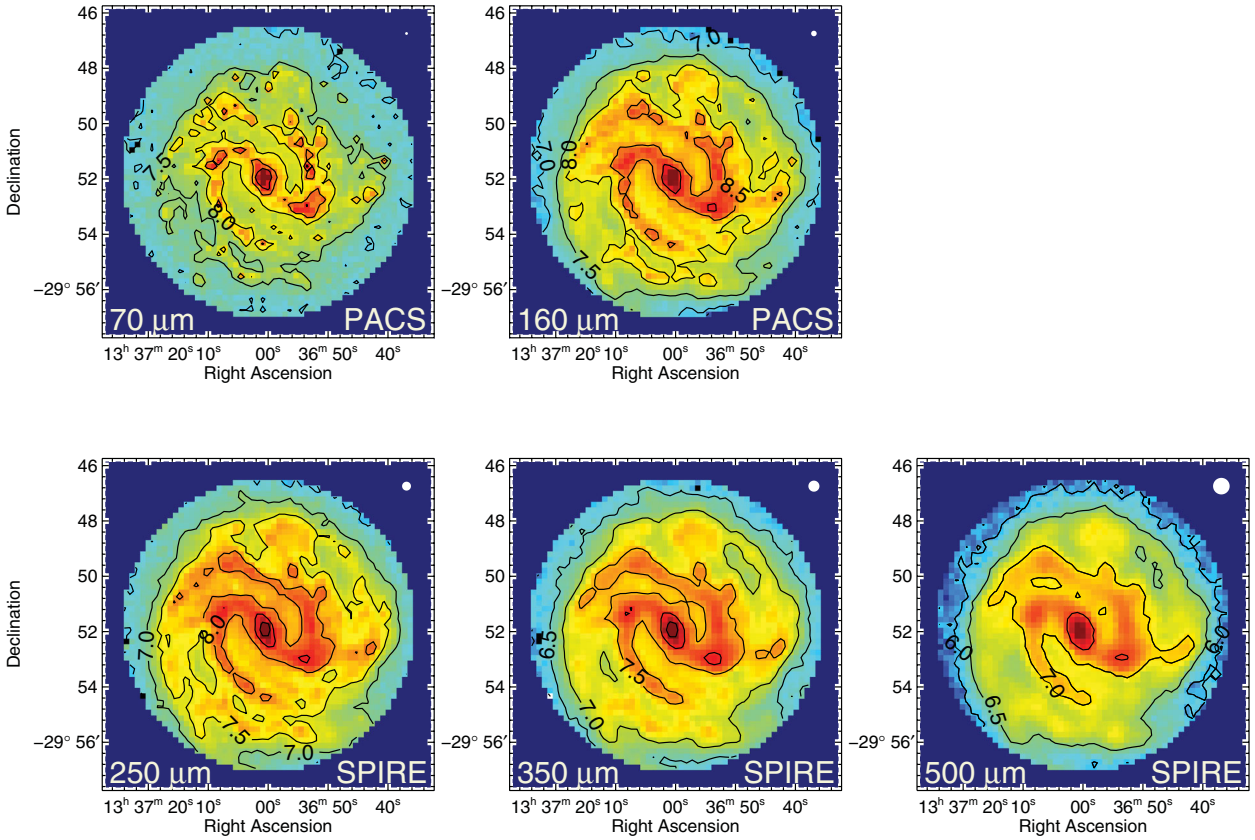

Figure 1. M83 at 70 and 160 μm imaged using PACS (upper panels, from left to right) and at 250, 350 and 500 μm imaged using SPIRE (lower panel, from left to right). The images are in Jy sr^{-1} and are scaled logarithmically with contours at equal increments (6, 6.5, 7, 7.5, 8, 8.5 and 9). The size of the PSF is illustrated in the top right-hand corner of each image (see Table 1 for pixel and PSF sizes).

Table 2. Adopted properties of M83.

Inclination	24°
Position angle	225°
Distance	4.5 Mpc

Muraoka et al. (2007) mapped CO ($J = 1 \rightarrow 0$) out to 3.5 kpc. However, archival CO ($J = 3 \rightarrow 2$) data from the JCMT (project: M06BN05) with a resolution of 14.5 arcsec allow us to map molecular gas distribution out to 5 kpc. Thus, we use the CO ($J = 3 \rightarrow 2$) but first scale the images to match the CO ($J = 1 \rightarrow 0$) of M83 using the ratio found by Muraoka et al. (2007), which varies with radius. Muraoka et al. (2007) found that the ratio of CO ($J = 3 \rightarrow 2$) to CO ($J = 1 \rightarrow 0$) intensity is as high as 1.0 in the very inner regions and decreases to 0.65 at 0.5 kpc. Beyond 0.5 kpc, the ratio is roughly constant at 0.65. We use a radially varying ratio, S. At each radial position, R, between 0 and 0.5 kpc, we have

$$S = 1.0 - 0.7R \qquad R < 0.5. \tag{1}$$

Beyond 0.5 kpc we use $S = 0.65$. Details on how the CO ($J = 3 \rightarrow 2$) images were processed can be found in Warren et al. (2010). We convert from antenna temperature to main beam temperature using a factor $\eta_{\rm MB} = 0.6$. To estimate the surface density of H_2 from CO, we then use a constant conversion factor of $X = 2.0 \times 10^{20}$ mol cm^{-2} (K km s^{-1})$^{-1}$ which corresponds to 3.2 $M_\odot$ pc^{-2} (K km s^{-1})$^{-1}$ (Wilson et al. 2009). We examine a conversion factor that varies with metallicity in Section 3.3. The H_2 maps are aligned and convolved to match the 500-μm images and are deprojected according to the values in Table 2.

Together the H I and H_2 maps are combined to make total gas surface density maps using a factor of 1.36 to account for helium.

2.3 SFR maps

Measuring the SFR requires accounting for both unobscured star formation and dust obscured star formation. In this work we use Hα images, which are corrected for dust obscuration in compact sources using 24-μm emission maps. We use continuum subtracted Hα images from Survey for Ionization in Neutral Gas Galaxies (SINGG; Meurer et al. 2006) and 24-μm observations from Engelbracht et al. (2005) that are reprocessed by Bendo et al. (2012, in preparation). The 24-μm emission traces star formation in compact regions that are obscured by dust, but also has a diffuse component from post-main-sequence stars. Here we exclude the diffuse component and only include the 24-μm emission from compact sources. Our goal is to trace star-forming regions rather than radiation associated with star formation. In Appendix B we compare our star formation tracer to linear combinations of images, which include the diffuse component.

Several authors have demonstrated that 24-μm emission from unresolved sources is correlated with the Hα emission from these sources (e.g. Calzetti et al. 2005, 2007; Prescott et al. 2007). Calzetti et al. (2007) derived the following equation to use 24-μm flux density measurements to correct the Hα flux from H II regions within

a galaxy to produce an extinction-corrected Hα flux:

$$f_{\mathrm{H}\alpha\ \mathrm{corrected}} = f_{\mathrm{H}\alpha\ \mathrm{observed}} + (0.031 \pm 0.006) f_{24\,\mu\mathrm{m}}. \quad (2)$$

We use the extinction-corrected Hα fluxes given by this equation as a star formation tracer in our analysis. However, to create a map of the extinction-corrected Hα emission, we first identify the unresolved Hα sources and their 24-μm counterparts. We then apply the correction to each source and re-map the extinction-corrected emission into a new map.

To identify the unresolved Hα sources, we used SExtractor (version 2.5.0; Bertin & Arnouts 1996) in double-image mode to create the initial source catalogues where detection and setting of apertures are done in the Hα image. All Hα images were first convolved to the resolution of the 24-μm image using a customized kernel created using the procedure outlined in Bendo et al. (2012). The images were then re-gridded to the pixel size of the 24-μm map. Sources were selected when at least 20 pixels were 3σ above the noise level in the Hα image used for detection. All photometry was measured in apertures with a 40 arcsec ($\sim$27 pixels) diameter. We used this fixed radius because it is larger than the peak in the second Airy ring of the 24-μm data and the aperture corrections should be less than or equal to the calibration uncertainties. To minimize the number of faint spurious sources in our catalogue, we exclude regions beyond the galaxy optical disc and foreground stars that appear as sources with positive and negative counterparts in the Hα images. We find that when run SExtractor is run in single-image mode, the mean absolute value difference between the 24-μm flux densities using the two methods is $\sim$13 per cent. Thus, we add a 13 per cent systematic error to all of the 24-μm measurements.

After performing these measurements, we corrected the Hα measurements for foreground dust extinction within the Milky Way using $A_R = 0.176$, which was calculated by the NASA/IPAC Extragalactic Database based on data from Schlegel, Finkbeiner & Davis (1998). We then applied equation (2) to calculate extinction-corrected Hα fluxes, re-mapped the Hα fluxes into individual pixels in a map with very small (1 arcsec) pixels, and then convolved the data with a Gaussian function with a FWHM of 36 arcsec to match the PSF of the 500-μm map for analysis.

Using the calibration of Kennicutt (1998) and Calzetti et al. (2007), we convert the corrected Hα maps, which we label as H$\alpha_{,\mathrm{cor}}$ into an SFR:

$$\mathrm{SFR}(\mathrm{M}_\odot\ \mathrm{yr}^{-1}) = 5.3 \times 10^{-42}\ L_{\mathrm{corr}}(\mathrm{H}\alpha_{,\mathrm{cor}})\ \mathrm{erg\ s}^{-1}. \quad (3)$$

For the remainder of this text, we will refer to the SFR using this description. In Appendix B we also compare this tracer to other tracers derived from a linear combination of images. We examine an SFR made from the combination of the far-ultraviolet (UV) and 24-μm emission as well as a combination of Hα and 24-μm emission across the whole image without the compact source identification outlined above.

All of the gas, dust and SFR maps are rebinned into 36-arcsec pixels corresponding to a physical size of 790 pc for the purposes of quantitative analysis (see Bendo et al. 2012, for a discussion). 36 arcsec represents the FWHM of the convolved data (see Table 1).

3 DUST MAPS

3.1 Temperature and emissivity

The dust temperature is determined by fitting each pixel in the PACS and SPIRE images with a single modified blackbody function of the form:

$$S_\lambda = N B_\lambda(T) \lambda^{-\beta}, \quad (4)$$

where S_λ is the flux density, $B_\lambda(T)$ is the Planck function, N is a constant related to the column density of the material and β is the emissivity. We fit the points using MPFIT, a least-squares curve fitting routine for IDL (Markwardt 2009). Because the dust emission does not have a flat spectrum across the bands, during our fitting routine, we apply colour corrections to the five images. The appropriate colour corrections were determined by first fitting the SED of the five images and determining the spectral index or slope at each point. The photometric colour corrections were determined by interpolation from the tables provided in the observer manuals of PACS and SPIRE. This process was repeated iteratively.

The grain emissivity parameter (β) of the dust reflects its properties and is important for determining the dust temperature and mass. Typically, it has a value of $\sim$2 (Draine & Lee 1984). However, it can vary from as low as 1 to as high as 3 (see Shetty et al. 2009a, and references therein). While constant values of β of either 1.5 or 2 have been used in many studies, β and the dust temperature may be anticorrelated due to the properties of amorphous grains (Dupac et al. 2001; Meny et al. 2007; Paradis et al. 2010). Thus, fixing β can lead to erroneous temperature values. However, noise and line-of-sight temperature variations can also produce this inverse relation making uncovering the intrinsic relation between β and temperature challenging (Shetty et al. 2009a,b; Malinen et al. 2011).

In this work we fit the dust emission using both a constant and a variable value of β. For a variable β we permit values between 1.0 (the limit of the Kramers–Kronig dispersion relation) and 2.5. The mean value of β over the entire galaxy is 2.1 ± 0.1. For our constant β fit, we assume a value of 2.0, which is close to the mean value found when β was allowed to vary. The mean χ^2 over all the fit pixels when using a variable β is 0.5 with a standard deviation of 0.3. In the case of a constant β the mean value is 0.7 with a standard deviation of 0.3. These χ^2 values are small suggesting that our errors may be large. This is likely due to the calibration errors, which are correlated. Fig. 2 shows four sample fits in log–log space for pixels in the nuclear, bar, spiral arm and interarm regions. The curves are all normalized to the peak value. The bottom panel shows how the data deviate from the fit (i.e. $\log S_\lambda - \log I_\lambda$). In each panel we list the fitted temperature and emissivity.

Fig. 3 shows the spatial distribution of β when it was allowed to vary (left) and the resulting temperature maps for a variable β (centre) and constant, $\beta = 2$ (right). The high β values on the edge of the map are likely due to the low signal-to-noise ratio in these regions. One notes clear differences in the two temperature maps, particularly in the inner regions. With a constant β, the central temperature peak is elongated perpendicular to the bar and shows an outer ring-like structure, whereas with a variable β the central peak is much more symmetrical. Over much of the galaxy, the value of β was close to 2, but in the inner regions there is a ring of higher β values. This ring is the source of the differences in the inner regions of the two temperature maps. Bendo et al. (2003) also found values of β close to 2 in the inner regions (within 135 arcsec) of M83 using *ISO* (Kessler et al. 1996) and SCUBA (Holland et al. 1999) data. M83 had the steepest emissivity law in their analysis of eight galaxies using a variable β.

Fig. 4 shows how β varies with temperature. There is an anti-correlation between β and temperature. This is in agreement with other studies (i.e. Dupac et al. 2001; Paradis et al. 2010; Dariush et al. 2011) and recent results from *Planck*, which have revealed

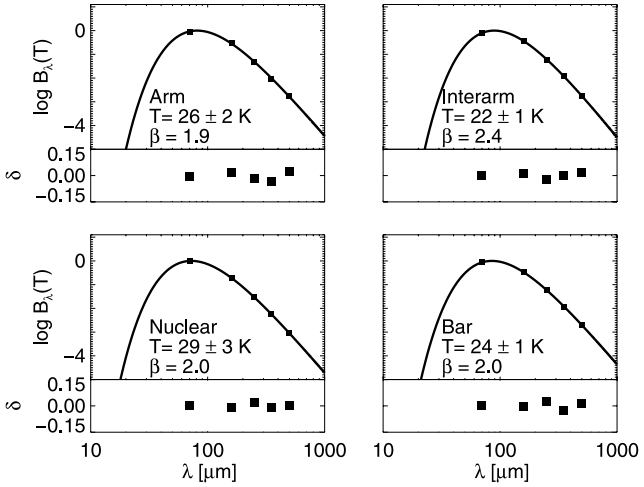

Figure 2. Sample modified blackbody fits for regions in the nucleus, bar, arm and interarm with the colour-corrected PACS and SPIRE points using a variable β (see centre of each panel for fit value). The peak of the function determines the temperature (listed in each panel). The functions are shown in log–log and are normalized to the peak of the function. The uncertainties are smaller than the symbol sizes. The deviation between each point and the fit (i.e. $\log S_\lambda - \log I_\lambda$) is shown below each panel.

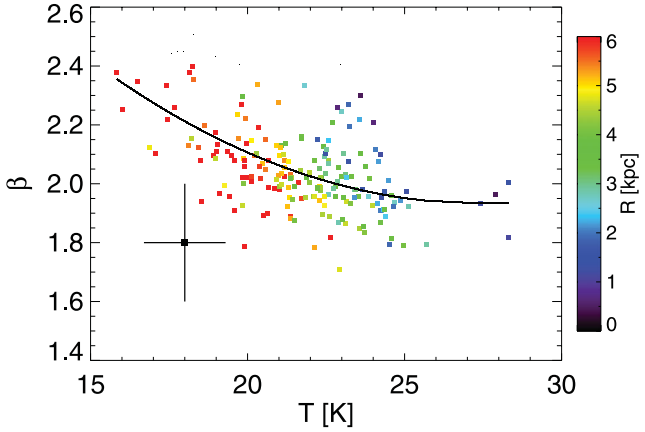

Figure 4. β versus temperature for the variable β SED fits. Each point represents a 36-arcsec region corresponding to the FWHM of the PSF in the convolved maps. The colours mark the radial position of the points with blue and green points within 3 kpc of the centre and yellow and red points extending further out. The black point illustrates the mean uncertainties of β and the temperature. The solid line shows the two-degree polynomial curve fit to the points, taking into consideration the uncertainties. We find that β and the temperature are anticorrelated in agreement with other studies. It is unclear whether this anticorrelation is intrinsic or is simply a reflection of noise and line-of-sight temperature variations (Shetty et al. 2009a,b).

an anticorrelation between β and temperature from SED fits of the integrated emission of nearby galaxies (Planck Collaboration et al. 2011).

However, whether we have uncovered the intrinsic inverse relation remains unclear as noise and line-of-sight temperature variations can also produce a similar relation (Shetty et al. 2009a,b). While there is a trend of decreasing β with increasing temperature, we note that in the inner regions (dark blue points) where there are mostly high temperatures ($T > 25$ K), there are some regions with β exceeding 2. These values lie in the ring-like structure seen in the left-hand panel of Fig. 3 and deviate from the anticorrelation. While it is possible that the ring is simply an artefact of imperfect PSF matching, it may also represent a region of different physical properties.

Using a single temperature modified blackbody fit means that at each pixel we have an average dust temperature. Typically, galaxies have a mixture of dust at different temperatures with a warmer and cooler component. Here we briefly examine to what extent these features might affect our results. In order to examine the possibility of a warmer component, we fit the SED with our constant β value of 2 dropping the 70-μm point. If the 70-μm point is higher than our fit using 160, 250, 350 and 500 μm, this suggests a warmer component (i.e. Bendo et al. 2010a; Smith et al. 2010). We find that the SED fit overpredicts the 70-μm value over much of the galaxy. This suggests that including the 70-μm point is necessary in order to properly constrain the peak. By examining the far-infrared colour variations in M83, Bendo et al. (2012) found that the dust could be

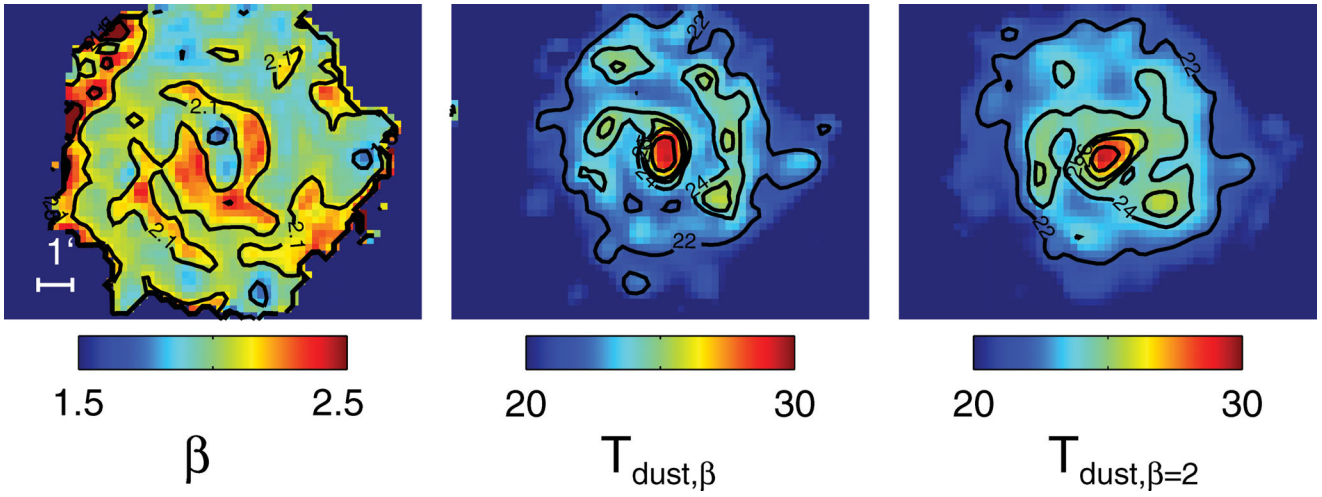

Figure 3. Spatial distribution of β (left), dust temperature using a variable β in the modified blackbody fit (centre) and dust temperature using a constant β of 2 in the modified blackbody fit (right). All three images show the same field of view. For scale we show a 1-arcmin distance on the deprojected images (left-hand panel). The contours in the β map are at 1.5, 1.8, 2.1 and 2.4. The contours in the two temperature maps (centre and right-hand panels) are the same and lie between 22 and 30 K in increments of 2. Over much of the galaxy the variable β is roughly 2. However, there is an inner ring of higher β values which leads to the differences in the central regions of the two temperature maps.

© 2012 The Authors, MNRAS **421,** 2917–2929
Monthly Notices of the Royal Astronomical Society © 2012 RAS

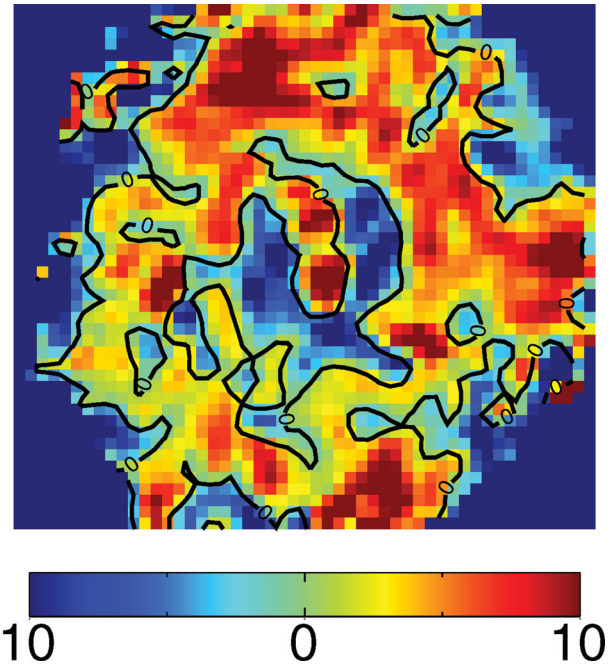

Figure 5. The per cent difference between the flux of the 500-μm map and that predicted by the fit using the 70-, 160-, 250- and 350-μm maps. Positive values mean the observed value is greater than predicted, while negative values mean the observed is less than predicted. With the exception of the inner ring, much of the galaxy shows an excess of 500-μm emission.

divided into a component radiating primarily at 250–500 μm and another at 70–160 μm, which is not evident in the test we perform here.

There may also be a cold dust component ($T \sim 5$–10 K), which has been attributed to a so-called 'submm excess' (i.e. Galliano et al. 2003, 2005; Bendo et al. 2006; Zhu et al. 2009; Gordon et al. 2010; O'Halloran et al. 2010). This submm excess has also been explained, in the case of the Milky Way, by wavelength-dependent variations in the dust emissivity (i.e. Reach et al. 1995; Paradis, Bernard & Mény 2009). Typically, one requires measurements at longer wavelengths (i.e. 850 μm) in order to identify the excess, but even at 500 μm the excess may present itself (i.e. Gordon et al. 2010). We repeat a similar procedure to that outlined above for the 70-μm observations. In general, we find that the 500 μm observed value exceeds the predicted value of the SED fit using the other four wavelengths by ∼10 per cent. This is in agreement with the excess found by Gordon et al. (2010). Fig. 5 shows the per cent difference between 500-μm (right) point and the fit using the other four maps. Positive values indicate an excess. We note that the regions where the 500 μm is underpredicted correspond to the ring-like structure in the variable β map. Since we were forced to keep β fix in order to properly fit the SED with only four points, this ring may be an artefact of fixing β. We stress that the excess found here is small in comparison to our uncertainties and longer wavelength measurements are necessary to confirm this finding.

3.2 Dust mass

We calculate the dust mass using the following equation at 250 μm:

$$M_{\rm dust} = \frac{S_{250} D^2}{\kappa_{250} B(\lambda_{250}, T)}, \quad (5)$$

where S_λ is the flux density from our SED fit at our chosen 250-μm wavelength (i.e. not the value in the 250-μm map), D is the distance to M83 (4.5 Mpc; Thim et al. 2003), $B(\lambda, T)$ is the Planck function using 250 μm and the best-fitting temperature and κ is the assumed emissivity. We use a κ of $2.72 \times 10^5\ (\lambda/\mu{\rm m})^{-2}\ {\rm cm}^2\ {\rm g}^{-1}$, where $\lambda = 250$ μm. The value of κ is taken from Li & Draine (2001) and modified with a correction discussed in Draine (2003).

We calculate the mass at 250 μm as it is not overly sensitive to the temperature like the shorter PACS wavelengths and has lower uncertainties than the other SPIRE wavelengths. We tested the other wavelengths as fiducial wavelengths for the dust mass maps and found that the total dust masses agree within the uncertainties.

We compared the spatial distribution of the dust surface density using either a constant β or variable β and found that they are very similar. We find a total dust mass of $4.0 \pm 0.6 \times 10^7\ {\rm M}_\odot$ with a variable β and $3.9 \pm 0.6 \times 10^7\ {\rm M}_\odot$ with a constant β within $r = 300$ arcsec. The difference between the two dust mass maps in individual pixels is at the 10 per cent level. Galametz et al. (2011) did global SED fits of M83 using infrared data from *IRAS* and submm data at 540 μm from Hildebrand et al. (1977). Without the submm data, they found a total dust mass of $8.5 \times 10^8\ {\rm M}_\odot$. However, when they included the submm data, the total dust mass decreased to $8.5 \times 10^6\ {\rm M}_\odot$, illustrating the need for longer wavelength data in order to properly constrain the SED fit. Our dust mass, while higher, is much closer to their global fit using the older longer wavelength data. We also compared the total dust mass from the fit, without using the 70- and 500-μm maps. In these cases, we assumed a β value of 2. In both cases, the total dust mass was identical to that using all five maps within the uncertainties. In Appendix A we also compare our dust mass estimations with those found using the models of Draine & Li (2007).

4 RESULTS AND DISCUSSION

4.1 Distribution of dust temperature and mass

Figs 3 and 6 show the dust temperature and dust mass surface density maps respectively for M83 based on the modified blackbody fits with a variable β. The highest temperatures (∼30 K) are found in the central peak, the spiral arms and the south-western bar–spiral arm transition. This is likely due to the increased star formation activity in these regions and, in the case of the bar end, orbit crowding of the molecular gas (Kenney & Lord 1991) and subsequent star formation activity. Regions outside of the nucleus but along the bar show lower temperatures, which are comparable to the temperatures in the interarm regions.

The dust mass surface density is shown in Fig. 6 in log solar masses per square parsec. The regions of highest dust concentration are located in the nucleus and at the ends of the bar. The right-hand panel shows the dust surface density with the temperature contours overlaid. The peak temperature in the south-western bar–spiral arm transition peak and the north-eastern spiral arm are offset from the dust mass surface density peaks. The dust temperature is highest ahead of the dust mass surface density arms if we assume a trailing spiral structure rotating in the clockwise direction. Dust temperature and mass maps for NGC 4501 and NGC 4567/8 in the *Herschel* Virgo Cluster Survey have also shown that the peaks in dust temperature were not coincident with those in mass (Smith et al. 2010).

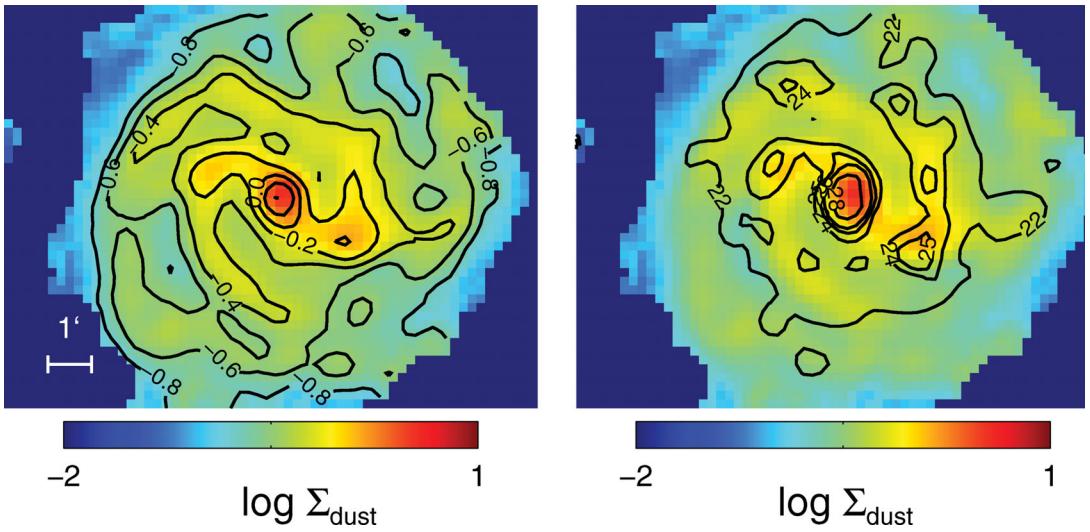

Figure 6. Dust mass surface density map in log $M_\odot\,pc^{-2}$ for M83 with contours (left) and with contours of the temperature map overlaid (right). The temperature map is that made with a variable β (see middle panel of Fig. 3). In many cases, peaks in temperature are offset ahead of peaks in mass in the spiral and bar structures.

4.2 Comparison with gas and SFR

We now compare the spatial distribution of the dust mass surface density and temperature with tracers of the atomic and molecular gas and the SFR. In Fig. 7 we show the tracers with contours of the dust surface density (upper panel) and contours of the dust temperature (lower panel). In Fig. 8 we plot the pixels in the dust mass surface density (upper row) and temperature maps (lower row) versus those in the different tracers. Each point represents an area of 36 arcsec (the FWHM of convolved beam) and we denote regions in the nucleus, bar and spiral arms in orange, purple and cyan, respectively. The choice for these regions was made by eye using 3.6-μm images from *Spitzer*'s IRAC camera (*Spitzer* Local Volume Legacy; Dale et al. 2009) that were convolved to the 500-μm resolution and deprojected. 3.6-μm maps roughly trace the underlying stellar mass density, which makes them well suited for probing morphological structures. Although PAH and hot dust emission can also contribute in this band in regions dominated by emission associated with star formation (Mentuch, Abraham & Zibetti 2010), since these regions in M83 already correspond to regions with enhanced stellar mass densities, this contamination does not affect our qualitative approach in decomposing the galaxy's morphology.

Examining the upper panel of Fig. 7, we see that peaks in the dust mass surface density are virtually coincident with those of the

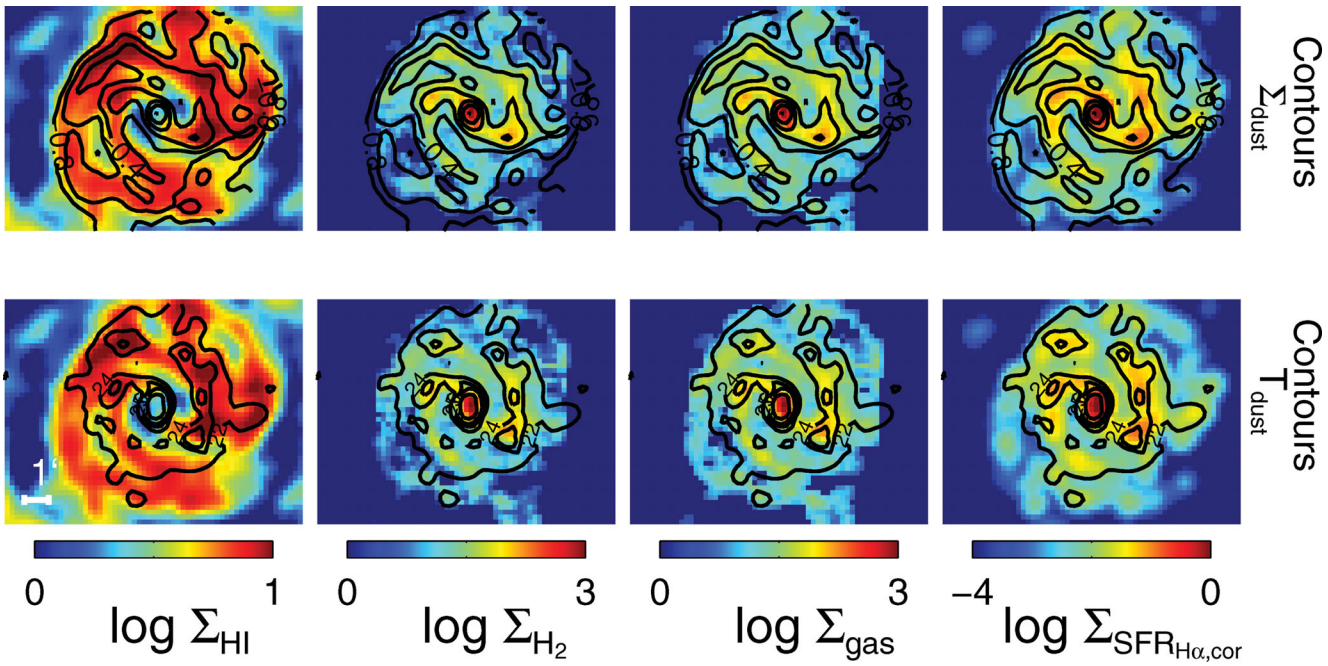

Figure 7. Atomic (left), molecular (second from left) and total (third from left) gas surface density (logarithmic scale) in $M_\odot\,pc^{-2}$ and the SFR (right) as determined from dust-corrected Hα emission (as described in Section 2.3) in $M_\odot\,kpc^{-2}\,yr^{-1}$. Contours of the dust mass surface density (upper panel) and temperature (bottom panel) distribution are overlaid. We find close agreement between the dust mass surface density and molecular gas and SFR distribution.

© 2012 The Authors, MNRAS **421,** 2917–2929
Monthly Notices of the Royal Astronomical Society © 2012 RAS

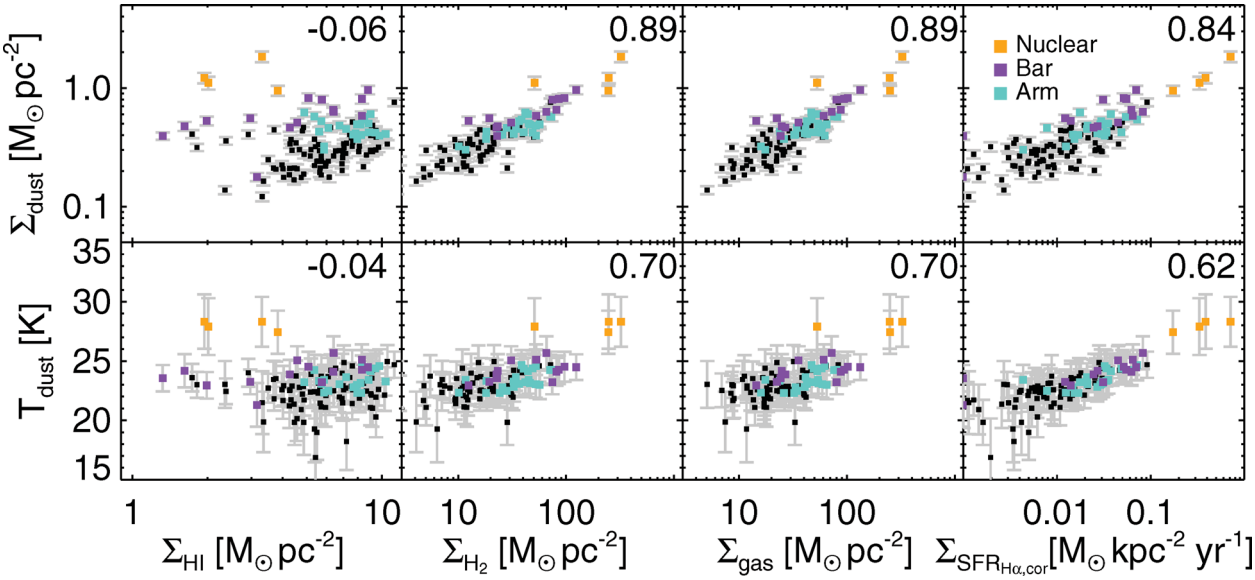

Figure 8. The dust temperature (lower panel) and dust mass surface density (upper panel) versus atomic gas (left), molecular gas (second from left), total gas (third from left) mass and the SFR (right) as traced by dust-corrected Hα emission. Each point represents a pixel 36 arcsec in size (the FWHM of the convolved maps). The pixels in the nucleus, bar and spiral arms are denoted in orange, purple and cyan, respectively. The black pixels are in the interarm region or are beyond the extent of the clearly defined spiral structure. The correlation coefficients between the different tracers are listed in the upper right of each panel. The dust mass surface density is tightly correlated with the molecular gas, total gas and SFR. The dust temperature is surprisingly only somewhat correlated with the SFR. While a rise in temperature is associated with increased molecular gas and SFR, the atomic gas mass is associated with a decrease in temperature.

molecular gas and the SFR. The position of the spiral arm structure in the dust mass surface density is also coincident with that in the atomic gas map. In the nucleus, however, we find little atomic gas. In contrast to the excellent spatial correspondence between the gas and SFR tracers with the dust mass surface density, we note that in the lower panel of Fig. 7 the dust temperature does not have as close of an agreement.

In Fig. 8 we examine in a more quantitative fashion the correlations between the dust and the different gas and SFR tracers (see the correlation coefficients in the upper right of each panel). Again here we find that the molecular gas is tightly correlated with the dust mass surface density. While the total gas is also tightly correlated with the dust surface density, it is important to note that over the radii considered, the molecular component dominates the mass budget (Crosthwaite et al. 2002), so this is not too surprising. We note that the dust temperature tends to increase with rising molecular gas and SFR, but remains flat with the atomic gas density. This is simply the result of the increasing atomic gas density with radius, but decreasing dust temperature with radius (see Fig. 9 for radial profiles). The dust temperature is somewhat correlated with the molecular gas and SFR, but the correlations are not as strong as with the dust mass surface density. Bendo et al. (2012) has also found offsets between colour temperatures (160/250 and 250/350) with the Hα spiral arm structure. This may reveal that while the dust mass surface density is tightly correlated to molecular clouds and thus, star formation, dust heating may be caused by a variety of sources and not just recent star formation activity. Stars form in dense, cold molecular clouds. After the stars have formed, they heat the surrounding dust that lies within one mean free path. Thus, it is possible that colder dust lies in the star-forming regions. As the dust disperses it will be heated by more stars in the surrounding region and will subsequently become hotter.

Examining the different regions of the galaxy reflected by the colour coding of the points, we find that the nuclear regions tend to have higher dust temperatures and higher dust masses for the same value of the gas surface density. The latter, however, may be due to radial variations in the gas-to-dust ratio (GDR) related to metallicity (see Section 4.5, for a further discussion of this).

4.3 Radial profiles

Fig. 9 shows the radial profiles of the gas tracers, SFR, dust temperature, dust mass surface density and dust emissivity profiles. Here again we mark the pixels in the nuclear (orange), bar (purple) and arm (cyan) regions based on the 3.6-μm map. The solid line denotes the azimuthal average using radial annuli of 12-arcsec width. The dashed lines show the standard deviation around the azimuthal average. The points represent 36-arcsec pixels.

The molecular gas profile of M83 (centre panel of Fig. 9) is typical of a strongly barred spiral galaxy. The profile shows a central peak of molecular gas that declines, but then rises again producing a 'shoulder'. The shoulder forms at the bar–spiral arm transition region (Nishiyama, Nakai & Kuno 2001) and is also seen in the SFR, dust temperature and dust mass surface density profiles. In investigating the UV extinction profiles of M83, Boissier et al. (2005) also found that the SFR and extinction rates were enhanced at the bar–spiral arm transition region.

We identified the peak of the shoulder in the different profiles by finding the first maximum beyond 1 kpc. It is marked in each plot by the dashed vertical line and it can also be seen in the transition from purple to cyan squares. The shoulder does not seem to be associated with the position of corotation, which is beyond the bar end for M83 and is marked in these plots with the solid vertical line at 3.7 kpc (Lundgren et al. 2004).

The shoulder is associated with high dust temperature and mass surface densities in the bar–spiral arm transition (especially the south-western arm) as seen in the spatial distribution maps in Section 4.1. The position of the shoulder varies with the different

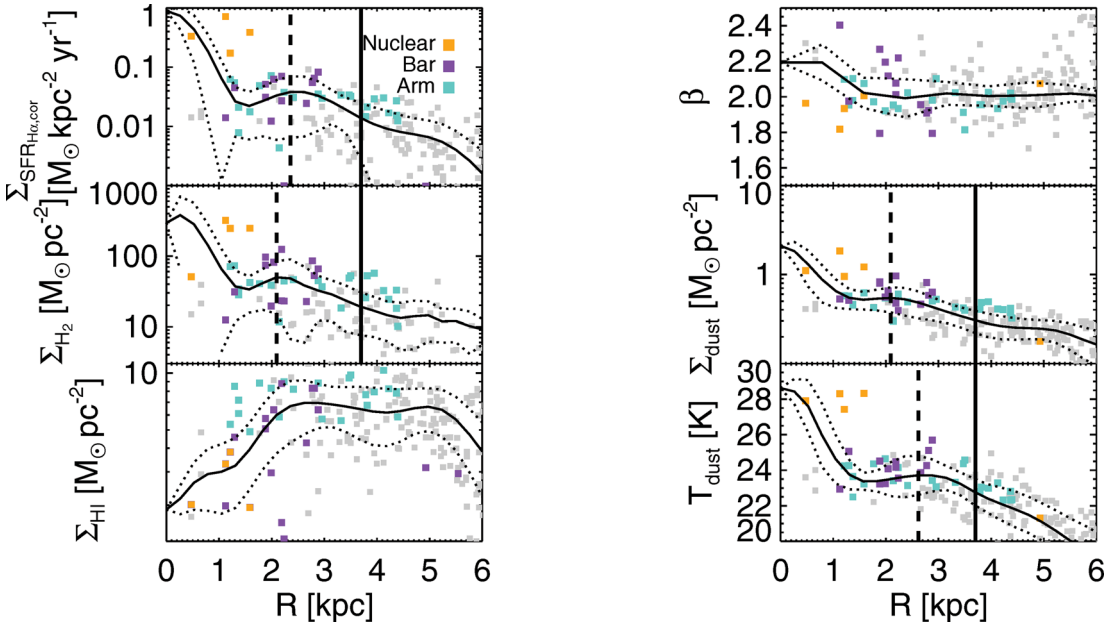

Figure 9. Radial profiles of the atomic gas (left, bottom), molecular gas (left, middle), SFR (left, top), dust temperature (right, bottom), dust mass surface density (right, middle) and emissivity, β values (right, top). The solid curve denotes the azimuthal average and the dotted lines show the standard deviation of this average. 36-arcsec pixels in the nuclear, bar and spiral regions are marked in orange, purple and cyan, respectively. Corotation and the shoulder position (vertical solid and dashed lines, respectively) are marked in the molecular gas, SFR, dust temperature and mass surface density panels.

Table 3. Shoulder position.

Profile	Shoulder position (kpc)
Dust temperature	2.9
Dust mass	2.1
SFR	2.4
Molecular gas	2.1

profiles (see Table 3 for the positions). The shoulders in the molecular gas and dust mass surface density profile are coincident. As we discussed in Section 4.3, there is close spatial agreement between the two maps. Both the dust temperature and SFR have shoulders that are further out in the disc, and surprisingly they are not coincident.

We note in the bottom-right panel Fig. 9 that the temperature of the dust in the bar region right before the shoulder is much higher than average (denoted by solid curve). This is likely due to increased SF due to orbit crowding in this region.

The top-right panel of Fig. 9 shows how the value of β varies with radius. β is close to 2 over much of the disc, with higher values in the inner 1 kpc.

4.4 Gas-to-dust ratio

Fig. 10 shows the radial variation of the GDR, which is derived using the total gas mass (atomic and molecular) divided by the dust mass. Both the azimuthal average (black solid line) and the region within the standard deviation (grey shaded area) are shown. Across M83 we find a mean value of 84 ± 4 (standard deviation: 40) which is roughly the galactic value of 100–200 (e.g. Sodroski et al. 1997). The right vertical panel of Fig. 10 shows the histogram of the GDR. Only a few regions in the galaxy have high GDRs in contradiction with previous estimates for M83 (Devereux & Young 1990) which did not probe the cold dust.

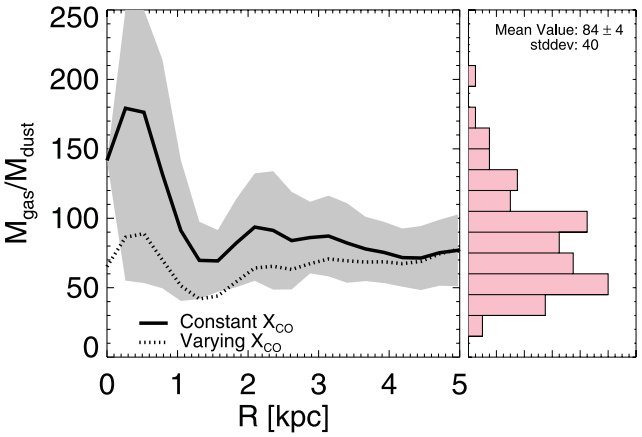

Figure 10. GDR versus radius (left) and histogram of the GDR (right). The azimuthal average of the GDR using a constant X_{CO} factor (solid line) and a radially varying one (dashed line) are shown. The grey shaded region shows the area within one standard deviation of the azimuthal average. The histogram is normalized to the peak value and the mean GDR and standard deviation are listed (upper right).

In the central regions, the GDR attains much higher values (over 200). This may simply be due to higher metallicities in the inner regions. One would expect a higher GDR with increasing metallicity. It may also be due to the X_{CO} factor which can often overestimate the molecular gas in the central regions of spiral galaxies including the Milky Way by a factor of 2 or more (i.e. Regan 2000).

The X_{CO} factor has been shown to be anticorrelated with metallicity in several studies (i.e. Wilson 1995; Arimoto, Sofue & Tsujimoto 1996; Boselli, Lequeux & Gavazzi 2002; Israel 2005). A recent study by Magrini et al. (2011) has shown that using an X_{CO} factor that varies with metallicity may have a large impact on the radial profile of the GDR. This is particularly true for the inner regions, where the molecular gas dominates.

© 2012 The Authors, MNRAS **421,** 2917–2929
Monthly Notices of the Royal Astronomical Society © 2012 RAS

In light of this, we recalculate our estimate of molecular hydrogen using an $X_{\rm CO}$ factor which varies with metallicity. Israel (2000) has derived a relationship between the $X_{\rm CO}$ factor and the oxygen abundance as

$$\log X_{\rm CO} = 12.2 - 2.5 \log \frac{\rm O}{\rm H}. \quad (6)$$

We use the oxygen abundance gradients of Bresolin et al. (2009), which are based on linear regression fits of the results of several strong-line studies in the outer regions of M83, and compiled studies of the inner region by Bresolin & Kennicutt (2002) and Bresolin et al. (2005). The abundance ratio decreases linearly from $12 + \log {\rm O/H} = 8.77$ in the centre to $12 + \log {\rm O/H} = 8.6$ at 6 kpc.

Fig. 10 shows the GDR using a variable $X_{\rm CO}$ factor (dashed line). One notes that the GDR in the inner regions are much reduced and there is now a slight trend towards an increasing GDR with radius. Some of the values in the inner region are much lower ($\sim$60) than the galactic value of 100–200. This may not be too surprising given that the metallicity of M83 is supersolar in the inner regions (Bresolin et al. 2005), which also implies higher dust masses and subsequently a lower GDR. This shows the sensitivity of the GDR to an $X_{\rm CO}$ factor that varies with metallicity.

The consistency of the GDR over much of the disc beyond the inner regions is in contradiction to several other studies of similarly nearby spiral galaxies. Recent studies of M99 and M100 (Pohlen et al. 2010) and NGC 2403 (Bendo et al. 2010b) have shown an increasing GDR with radius. Muñoz-Mateos et al. (2009) also showed that almost all galaxies in the *Spitzer* Infrared Nearby Galaxy Survey (SINGS; Kennicutt et al. 2003) sample showed radially increasing GDRs. However, there were two exceptions. NGC 3627 showed a decreasing GDR and NGC 2976 showed a fairly consistent GDR.

5 CONCLUSIONS

The close proximity of M83 has allowed us to probe in detail the dust temperature and mass distribution using images from PACS and SPIRE. With its prominent bar and spiral arms, we have also been able to compare different environments and see the correspondence of the dust temperature and mass with tracers of the gas and SFR. We briefly summarize our findings.

(i) We find an anticorrelation between β and temperature with a mean value of β of 2.1 ± 0.1. However, it is possible this anticorrelation is an artefact of noise and line-of-sight temperature variations (Shetty et al. 2009a,b). A comparison of the dust temperature maps made using a constant $\beta = 2$ and a variable β shows that the most prominent differences are in the inner regions. The dust mass surface density maps are virtually identical and have the same total dust mass within the uncertainties.

(ii) We find a total dust mass of $4.0 \pm 0.6 \times 10^7$ M$_\odot$.

(iii) We find that the dust temperature and mass surface density distributions are not spatially coincident. In particular, while the dust mass surface density correlates extremely well with the molecular gas and SFR, we find that the dust temperature peaks are offset. In the spiral arms, we find that the dust temperature peaks lie ahead of the dust mass surface density (assuming a trailing spiral structure).

(iv) The dust temperature is more strongly correlated with the molecular gas than the SFR.

(v) The nuclear and bar–arm transition regions show enhanced dust mass surface densities and temperature. The bar–arm transition regions lead to the development of a 'shoulder' in the radial profile plots. The position of the shoulder varies between the dust mass surface density and temperature radial profiles.

(vi) The GDR has a mean value of 84 ± 4, which is close to the galactic value. In the inner regions the GDR extends as high as 200.

(vii) Using an $X_{\rm CO}$ factor that varies with metallicity decreases the GDR in the inner regions.

ACKNOWLEDGMENTS

KF acknowledges helpful conversations with Brent Groves, Frank Israel, Adam Leroy, Giovanni Natale, Karin Sandstrom and Ramin Skibba. This research was supported by grants from the Canadian Space Agency and the National Science and Engineering Research Council of Canada (PI: C. Wilson). PACS has been developed by a consortium of institutes led by MPE (Germany) and including UVIE (Austria); KU Leuven, CSL, IMEC (Belgium); CEA, LAM (France); MPIA (Germany); INAF-IFSI/OAA/OAP/OAT, LENS, SISSA (Italy) and IAC (Spain). This development has been supported by the funding agencies BMVIT (Austria), ESA-PRODEX (Belgium), CEA/CNES (France), DLR (Germany), ASI/INAF (Italy) and CICYT/MCYT (Spain). SPIRE has been developed by a consortium of institutes led by Cardiff University (UK) and including University of Lethbridge (Canada); NAOC (China); CEA, LAM (France); IFSI, University of Padua (Italy); IAC (Spain); Stockholm Observatory (Sweden); STFC and UKSA (UK); Imperial College London, RAL, UCL-MSSL, UKATC, University of Sussex (UK) and Caltech, JPL, NHSC, University of Colorado (USA). This development has been supported by national funding agencies: CSA (Canada); NAOC (China); CEA, CNES, CNRS (France); ASI (Italy); MCINN (Spain); SNSB (Sweden); STFC (UK) and NASA (USA). HIPE is a joint development by the Herschel Science Ground Segment Consortium, consisting of ESA, the NASA Herschel Science Center, and the HIFI, PACS and SPIRE consortia. This research has made use of the NASA/IPAC Extragalactic Database (NED) which is operated by the Jet Propulsion Laboratory, California Institute of Technology, under contract with the National Aeronautics and Space Administration.

REFERENCES

Aniano G., Draine B. T., Gordon K. D., Sandstrom K., 2011, PASP, 123, 1218
Arimoto N., Sofue Y., Tsujimoto T., 1996, PASJ, 48, 275
Bendo G. J. et al., 2003, AJ, 125, 2361
Bendo G. J. et al., 2006, ApJ, 652, 283
Bendo G. J. et al., 2010a, A&A, 518, L65
Bendo G. J. et al., 2010b, MNRAS, 402, 1409
Bendo G. J. et al., 2012, MNRAS, 419, 1833
Bertin E., Arnouts S., 1996, A&AS, 117, 393
Boissier S. et al., 2005, ApJ, 619, L83
Boselli A., Lequeux J., Gavazzi G., 2002, A&A, 384, 33
Bresolin F., Kennicutt R. C., Jr, 2002, ApJ, 572, 838
Bresolin F., Schaerer D., González Delgado R. M., Stasińska G., 2005, A&A, 441, 981
Bresolin F., Ryan-Weber E., Kennicutt R. C., Goddard Q., 2009, ApJ, 695, 580
Calzetti D. et al., 2005, ApJ, 633, 871
Calzetti D. et al., 2007, ApJ, 666, 870
Crosthwaite L. P., Turner J. L., Buchholz L., Ho P. T. P., Martin R. N., 2002, AJ, 123, 1892
Dale D. A. et al., 2007, ApJ, 655, 863
Dale D. A. et al., 2009, ApJ, 703, 517
Dariush A. et al., 2011, MNRAS, 418, 64
Devereux N. A., Young J. S., 1990, ApJ, 359, 42
Dowell C. D. et al., 2003, Proc. SPIE, 4855, 73
Draine B. T., 2003, ARA&A, 41, 241

Draine B. T., Lee H. M., 1984, ApJ, 285, 89
Draine B. T., Li A., 2007, ApJ, 657, 810
Draine B. T. et al., 2007, ApJ, 663, 866
Dunne L., Eales S. A., 2001, MNRAS, 327, 697
Dunne L., Eales S., Edmunds M., Ivison R., Alexander P., Clements D. L., 2000, MNRAS, 315, 115
Dupac X. et al., 2001, ApJ, 553, 604
Engelbracht C. W., Gordon K. D., Rieke G. H., Werner M. W., Dale D. A., Latter W. B., 2005, ApJ, 628, L29
Galametz M., Madden S. C., Galliano F., Hony S., Bendo G. J., Sauvage M., 2011, A&A, 532, A56
Galliano F., Madden S. C., Jones A. P., Wilson C. D., Bernard J.-P., Le Peintre F., 2003, A&A, 407, 159
Galliano F., Madden S. C., Jones A. P., Wilson C. D., Bernard J.-P., 2005, A&A, 434, 867
Gil de Paz A. et al., 2007, ApJS, 173, 185
Gordon K. D. et al., 2010, A&A, 518, L89
Griffin M. J. et al., 2010, A&A, 518, L3
Hildebrand R. H., Whitcomb S. E., Winston R., Stiening R. F., Harper D. A., Moseley S. H., 1977, ApJ, 216, 698
Holland W. S. et al., 1999, MNRAS, 303, 659
Israel F., 2000, in Combes F., Pineau Des Forets G., eds, Molecular Hydrogen in Space. Cambridge Univ. Press, Cambridge, p. 293
Israel F. P., 2005, A&A, 438, 855
Kenney J. D. P., Lord S. D., 1991, ApJ, 381, 118
Kennicutt R. C., Jr, 1998, ApJ, 498, 541
Kennicutt R. C., Jr, et al., 2003, PASP, 115, 928
Kennicutt R. C., Jr, et al., 2009, ApJ, 703, 1672
Kessler M. F. et al., 1996, A&A, 315, L27
Knapen J. H., Sharp R. G., Ryder S. D., Falcón-Barroso J., Fathi K., Gutiérrez L., 2010, MNRAS, 408, 797
Leroy A. K., Walter F., Brinks E., Bigiel F., de Blok W. J. G., Madore B., Thornley M. D., 2008, AJ, 136, 2782
Li A., Draine B. T., 2001, ApJ, 554, 778
Liu G., Koda J., Calzetti D., Fukuhara M., Momose R., 2011, ApJ, 735, 63
Lord S. D., Kenney J. D. P., 1991, ApJ, 381, 130
Lundgren A. A., Olofsson H., Wiklind T., Rydbeck G., 2004, A&A, 422, 865
Magrini L. et al., 2011, A&A, 535, A13
Malinen J., Juvela M., Collins D. C., Lunttila T., Padoan P., 2011, A&A, 530, A101
Markwardt C. B., 2009, in Bohlender D. A., Durand D., Dowler P., eds, ASP Conf. Ser. Vol. 411, Astronomical Data Analysis Software and Systems XVIII. Astron. Soc. Pac., San Francisco, p. 251
Mentuch E., Abraham R. G., Zibetti S., 2010, ApJ, 725, 1971
Meny C., Gromov V., Boudet N., Bernard J.-P., Paradis D., Nayral C., 2007, A&A, 468, 171
Meurer G. R. et al., 2006, ApJS, 165, 307
Muñoz-Mateos J. C. et al., 2009, ApJ, 701, 1965
Muraoka K. et al., 2007, PASJ, 59, 43
Nishiyama K., Nakai N., Kuno N., 2001, PASJ, 53, 757
O'Halloran B. et al., 2010, A&A, 518, L58
Paradis D., Bernard J.-P., Mény C., 2009, A&A, 506, 745
Paradis D. et al., 2010, A&A, 520, L8
Pilbratt G. L. et al., 2010, A&A, 518, L1
Planck Collaboration et al., 2011, A&A, 536, A16
Poglitsch A. et al., 2010, A&A, 518, L2
Pohlen M. et al., 2010, A&A, 518, L72
Prescott M. K. M. et al., 2007, ApJ, 668, 182
Rand R. J., Lord S. D., Higdon J. L., 1999, ApJ, 513, 720
Reach W. T. et al., 1995, ApJ, 451, 188
Regan M. W., 2000, ApJ, 541, 142
Rieke G. H. et al., 2004, ApJS, 154, 25
Roussel H., 2012, A&A, submitted
Schlegel D. J., Finkbeiner D. P., Davis M., 1998, ApJ, 500, 525
Shetty R., Kauffmann J., Schnee S., Goodman A. A., Ercolano B., 2009a, ApJ, 696, 2234
Shetty R., Kauffmann J., Schnee S., Goodman A. A., 2009b, ApJ, 696, 676
Smith M. W. L. et al., 2010, A&A, 518, L51
Sodroski T. J., Odegard N., Arendt R. G., Dwek E., Weiland J. L., Hauser M. G., Kelsall T., 1997, ApJ, 480, 173
Thim F., Tammann G. A., Saha A., Dolphin A., Sandage A., Tolstoy E., Labhardt L., 2003, ApJ, 590, 256
Tilanus R. P. J., Allen R. J., 1993, A&A, 274, 707
Vogler A., Madden S. C., Beck R., Lundgren A. A., Sauvage M., Vigroux L., Ehle M., 2005, A&A, 441, 491
Walter F., Brinks E., de Blok W. J. G., Bigiel F., Kennicutt R. C., Jr, Thornley M. D., Leroy A., 2008, AJ, 136, 2563
Warren B. E. et al., 2010, ApJ, 714, 571
Werner M. W. et al., 2004, ApJS, 154, 1
Wilson C. D., 1995, ApJ, 448, L97
Wilson C. D. et al., 2009, ApJ, 693, 1736
Zhu M., Papadopoulos P. P., Xilouris E. M., Kuno N., Lisenfeld U., 2009, ApJ, 706, 941

APPENDIX A: COMPARISON WITH DRAINE & LI MODELS

We compare our dust mass estimation using the modified blackbody analysis with that found using the models from Draine & Li (2007) and the five PACS and SPIRE images. The models are fitted using the two-component emission model put forth by Draine & Li (2007). In their model, the mid- through far-infrared emission due to PAHs, very small dust grains and carbonaceous dust grains is expressed as a function of the underlying interstellar radiation field (ISRF). The ISRF is represented by two components, one consisting of an emission component modelling a photodissociation region (PDR) with a range of starlight intensities from $U = U_{\rm min}$ to 10^6 and an interstellar medium component with a single radiation field of $U = U_{\rm min}$.[4] The bulk of dust mass is contained in this latter component. In our least-squares fitting procedure, $U_{\rm min}$ ranged from 0.1 to 25 and we vary the fraction, γ, of the PDR to total emission from 10^{-2} to 1. We fix the PAH fraction, $q_{\rm pah}$, to 4.58, common for solar to subsolar metallicity spiral galaxies (Draine et al. 2007). Errors are computed by generating 100 realizations of the photometry using a standard Monte Carlo simulation. We find a total dust mass of $5.3 \pm 1.0 \times 10^7$ M$_\odot$, which is factor of $\sim$1.3 greater than a modified blackbody dust mass with $\beta = 2$. The distribution of the dust mass surface density is similar with that found by the modified blackbody fit; in addition, the $U_{\rm min}$ map is similar to the temperature map using a constant β. Fig. A1 shows both the dust surface density (left) and $U_{\rm min}$ distribution using the Draine & Li (2007) models.

We find that an enhanced γ can fit the photometry in the nuclear region and the arms, although our variance in these fitted parameters is larger than the fitted parameters themselves and thus also gives a result consistent with requiring no PDR region. $U_{\rm min}$ is highest in the nuclear region (mean value in nucleus: 11 ± 5; maximum value in nucleus: 18 ± 8) and enhanced along the spiral arms (mean value in spiral arms: 5 ± 1). We also find a similar offset between the peaks in $U_{\rm min}$ and the dust mass as we have found between the dust mass and temperature for the modified blackbody model fits.

APPENDIX B: COMPARISON OF SFR TRACERS

In this work we used an SFR tracer that was derived from an Hα map using a 24-μm map for compact source corrections (see Section 2.3). This tracer is developed by implicitly assuming that the diffuse

[4] We adopt the notation of Draine & Li (2007).

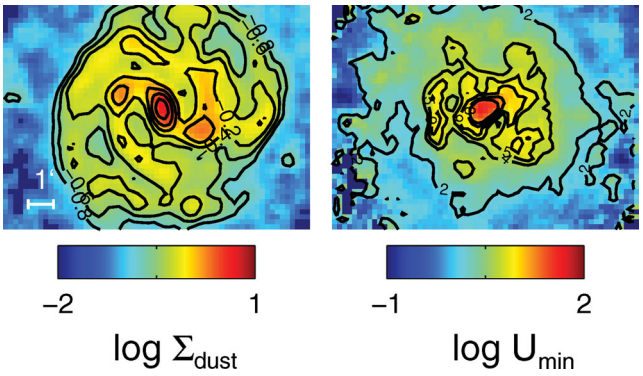

Figure A1. Dust mass surface density in log $M_\odot\,pc^{-2}$ (left) and U_{min} (right) based on fits using the Draine & Li (2007) models. While the dust mass surface density map looks very similar to that made with the modified blackbody fit, the surface densities are all approximately 1.5 times higher (see Fig. 6). The U_{min} map shows similar features to the dust temperature map derived from a modified blackbody fit with a constant β (see Fig. 3).

24-μm emission is not associated with recent star formation and thus should be removed (i.e. we only use the 24-μm emission as a compact source correction). We now examine how these results compare to using an SFR tracer that is a linear combination of two maps and thus includes this diffuse emission. There are many ways to trace sites of star formation, and here we explore two alternative descriptions using a combination of the far-ultraviolet (UV) from *GALEX* (Gil de Paz et al. 2007) and 24 μm from Engelbracht et al. (2005) as described by Leroy et al. (2008) and a linear combination of Hα and 24 μm (Calzetti et al. 2007). We first briefly describe the image rendering for this analysis.

In order to make the $SFR_{UV+24\,\mu m}$, we convolved the UV and 24-μm maps to the 500-μm resolution and deprojected them in accordance with Table 2. The UV and 24-μm images are combined

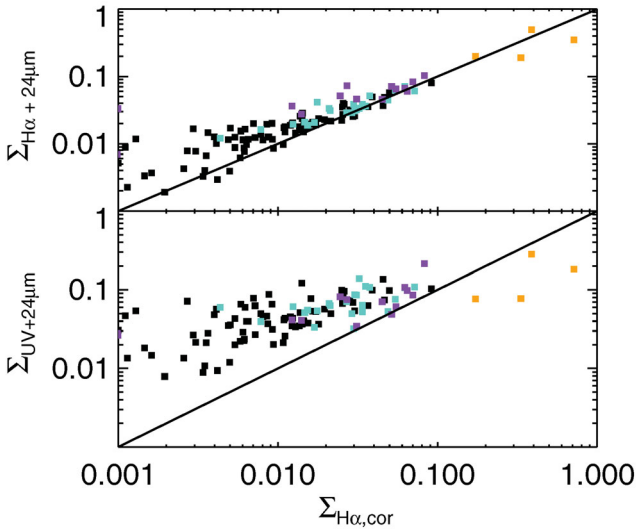

Figure B1. SFR as traced by a linear combination of maps [UV + 24 μm (bottom panel) and Hα + 24 μm (top panel)] versus a star formation tracer of $H\alpha_{,cor}$ with a compact source correction using 24 μm. Each point represents a pixel of 36 arcsec.

in the following fashion:

$$\Sigma_{SFR} = (8.1 \times 10^{-2} I_{UV} + 3.2 \times 10^{-3} I_{24}), \quad \text{(B1)}$$

where Σ_{SFR} has units of $M_\odot\,kpc^{-2}\,yr^{-1}$ and the UV and 24-μm intensity are each in MJy sr^{-1} (for more details, see appendix A of Leroy et al. 2008).

For the $SFR_{H\alpha+24\,\mu m}$, we convolve each map to the 500 μm and deproject them in accordance with Table 2. The Hα map is corrected for foreground dust extinction in the Milky Way as previously described in Section 2.3. Rather than applying the 24-μm correction

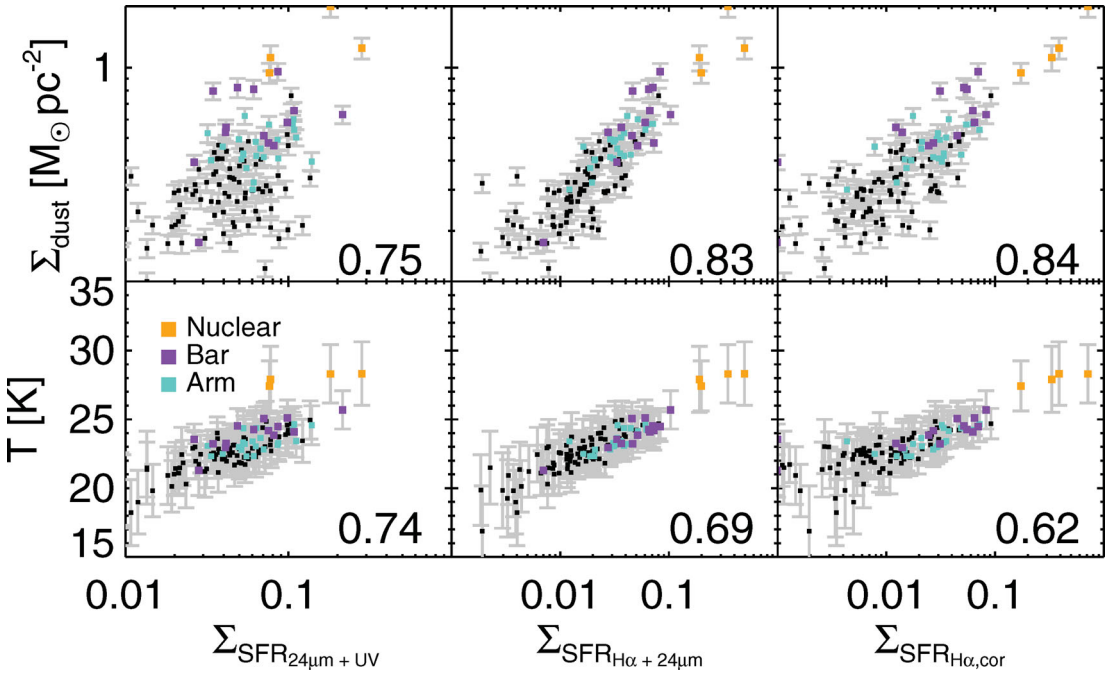

Figure B2. Dust mass surface density (upper panel) and dust temperature (lower panel) versus the SFR as traced by a linear combination of UV and 24 μm (left), Hα and 24 μm (centre) and $H\alpha_{,cor}$ with a 24 μm correction for compact sources (right). Each point represents a pixel of 36 arcsec. The correlation coefficients are listed in the bottom right of each panel.

to H II regions within the galaxy, we simply combine the two maps using

$$f_{\mathrm{H}\alpha+24\,\mu\mathrm{m}} = f_{\mathrm{H}\alpha} + (0.031) f_{24\,\mu\mathrm{m}}. \quad \text{(B2)}$$

We then convert this into an SFR using equation (2) (see Section 2.3) and convert this into an SFR surface density.

Fig. B1 provides a direct comparison of the tracers. On the *x*-axis we plot the SFR used throughout the text, namely $\mathrm{H}\alpha_{,\mathrm{cor}}$ with a compact source correction using 24-μm emission. For simplicity we refer to this simply as Hα. On the *y*-axis we plot the SFR based on the linear combination of two tracers with the UV + 24 μm on the bottom panel and Hα + 24 μm on the top panel. In both cases, the linear combination overestimates the SFR at low values of the SFR, with the greatest overestimates being for the UV + 24 μm.

As clearly stated in Kennicutt et al. (2009), while a linear combination of Hα + 24 μm may be an appropriate description for the SFR as a global quantity, for spatially resolved measures, errors will be introduced. Due to diffuse dust emission caused by dust heating of older stars, some regions will obtain 'spuriously high SFRs where little or no star formation is taking place' (Kennicutt et al. 2009). For the UV + 24 μm tracer, there is also the diffuse UV component and the longer time-scale for the UV emission (∼100 Myr) in comparison to Hα (∼40 Myr) (see Liu et al. 2011, for a discussion and comparison of these tracers).

In Fig. B2 we plot dust mass surface density and dust temperature versus SFR tracer. We also calculate the correlation coefficients between the different pairs. In the case of dust surface density, we find the correlation coefficients to be 0.75, 0.83 and 0.84 between the UV + 24 μm, Hα + 24 μm and the $\mathrm{H}\alpha_{,\mathrm{cor}}$ with a compact source correction, respectively. In other words, the dust surface density is most strongly correlated with the SFR used in this paper. In the case of the dust temperature, we find an opposite ordering of the correlation coefficients with 0.74, 0.69 and 0.62 for UV + 24 μm, Hα + 24 μm and the $\mathrm{H}\alpha_{,\mathrm{cor}}$ with a compact source correction, respectively. This suggests that the tracers composed of linear combinations of maps are capturing a diffuse heating component since they are more strongly correlated with dust temperature rather than dust mass surface density, which is coupled to molecular clouds and subsequent star formation activity. Thus, the concern that the diffuse 24-μm emission is not tracing recent star formation seems to be valid based on these findings.

This paper has been typeset from a TEX/LATEX file prepared by the author.

© 2012 The Authors, MNRAS **421,** 2917–2929
Monthly Notices of the Royal Astronomical Society © 2012 RAS